Please cite this article in press as: Amoudruz et al., The stress-free state of human erythrocytes: Data-driven inference of a transferable RBC model, Biophysical Journal (2023), https://doi.org/10.1016/j.bpj.2023.03.019

Biophysical Journal
Article

Biophysical Society

The stress-free state of human erythrocytes: Data-driven inference of a transferable RBC model

Lucas Amoudruz,[1,2] Athena Economides,[1,2] Georgios Arampatzis,[1,2] and Petros Koumoutsakos[1,2,*]
[1]Computational Science and Engineering Laboratory, ETH Zürich, Zürich, Switzerland and [2]School of Engineering and Applied Sciences, Harvard University, Cambridge, Massachusetts

ABSTRACT The stress-free state (SFS) of red blood cells (RBCs) is a fundamental reference configuration for the calibration of computational models, yet it remains unknown. Current experimental methods cannot measure the SFS of cells without affecting their mechanical properties, whereas computational postulates are the subject of controversial discussions. Here, we introduce data-driven estimates of the SFS shape and the visco-elastic properties of RBCs. We employ data from single-cell experiments that include measurements of the equilibrium shape of stretched cells and relaxation times of initially stretched RBCs. A hierarchical Bayesian model accounts for these experimental and data heterogeneities. We quantify, for the first time, the SFS of RBCs and use it to introduce a transferable RBC (t-RBC) model. The effectiveness of the proposed model is shown on predictions of unseen experimental conditions during the inference, including the critical stress of transitions between tumbling and tank-treading cells in shear flow. Our findings demonstrate that the proposed t-RBC model provides predictions of blood flows with unprecedented accuracy and quantified uncertainties.

SIGNIFICANCE Red blood cells (RBCs) are the dominant constituents of blood and their dynamics is governed by the visco-elastic properties of their membrane. Existing RBC models rely on the assumption of a stress-free state (SFS) of the cytoskeleton. This state is arbitrarily selected and current experimental methods cannot measure it directly. Essentially RBC models are not transferable and their parameters are adapted arbitrarily across flow configurations. Here, we introduce a transferable RBC (t-RBC) model parameterized by the SFS and the visco-elastic properties of the membrane. The model is calibrated from single-cell experiments using Bayesian inference. The t-RBC model is shown to reproduce a wide range of experimental data without further calibration of its parameters.

INTRODUCTION

Red blood cells (RBCs) are vital elements of blood as they are responsible for the delivery of oxygen to the entire human body. As they traverse the microcirculature, RBCs undergo highly non-linear deformations, which are accommodated by their visco-elastic properties (2). These properties are mainly controlled by the structure of their membrane, composed of a lipid bilayer anchored on a network of proteins (cytoskeleton) and enclosing a viscous solvent (hemoglobin). The RBC membrane and the hemoglobin are both considered incompressible. The cytoskeleton and the lipid bilayer of the membrane provide elastic resistance against local shearing, stretching, and bending. Over the last two decades, numerous mathematical models for the RBC membrane have been proposed, aiming to explain complex phenomena and complement experimental studies through parametric exploration and system optimization (3).

State-of-the-art models of RBCs account for shear deformation of the membrane with respect to a state at which the membrane has zero in-plane elastic energy, namely the stress-free state (SFS) (4–9). The existence of a non-spherical SFS was demonstrated by the experimental results of Fischer (10), who showed that the RBC membrane exhibits shape memory, and of Dupire et al. (11), who suggested that shape memory can explain certain dynamical transitions of cells in shear flow. Švelc and Svetina (12) suggested an analysis to compare the deformation of the cytoskeleton in a micropipette for a given SFS shape with that measured by experiments (13) but did not infer the SFS from the experimental data. Furthermore, current experimental

Submitted June 21, 2022, and accepted for publication March 10, 2023.
*Correspondence: petros@seas.harvard.edu
Editor: Timo Betz.
https://doi.org/10.1016/j.bpj.2023.03.019

Please cite this article in press as: Amoudruz et al., The stress-free state of human erythrocytes: Data-driven inference of a transferable RBC model, Biophysical Journal (2023), https://doi.org/10.1016/j.bpj.2023.03.019

methods do not allow us to directly measure the SFS of cells without affecting their mechanical properties (see section 2.3.3 of Lim et al. (4) and references therein). For these reasons, previous authors have performed parametric studies using a predefined SFS. Such calibrations affect the dynamics of RBCs, and in turn are key factors when comparing computational and experimental data (4,6,7,14,15). An ever-increasing amount of evidence from both experiments and simulations have shown that the SFS of the membrane skeleton is neither a biconcave resting shape nor a spherical shell (6,7,15). The consensus on the SFS is an oblate-like shell, with the same surface area and a larger volume than the RBC, although the exact SFS remains elusive (6,7,14).

Several computational studies have performed parametric investigations to quantify the effect of the SFS on the response of RBCs, under static and dynamic conditions (4,6,7,15–17). The SFS calibration shape was shown to significantly affect predictions of the RBC dynamics in simple shear flow. In particular, computational findings (6,7) demonstrated that the SFS alters not only the critical shear rate separating tumbling and tank-treading RBC dynamics but also the motion of the RBC membrane at the critical shear rate. Peng et al. (7) searched for a family of SFSs that could reproduce at the same time the biconcave resting shape and the dynamics of single erythrocytes in simple shear flow. Their findings show that an SFS closer to a sphere, rather than to a biconcave disk, not only approaches the experimental critical shear stress but also preserves the experimentally observed biconcave shape during tank treading (11). This finding was in contrast to previous computational studies. As a result, Peng et al. (7) envisioned that RBC dynamics at low shear rates might enable the quantification of the SFS.

We complement the aforementioned studies by performing a data-driven inference of the SFS and its potential variability in the population of healthy RBCs. We use hierarchical Bayesian inference to integrate data from multiple experimental sources and conditions and generate a data-informed probabilistic RBC model that incorporates modeling and experimental uncertainties in its predictions (1). The structure of the model incorporates the variability (18) of RBCs' elastic properties. In contrast to the recent study by Economides et al. (1), where the RBC model was considered a "black box" with an arbitrary, predefined SFS, here we perform a global sensitivity analysis for each quantity of interest. Inert factors are excluded during the inference process to reduce the computational cost and avoid numerical artifacts while sampling the posterior distribution (19). The high computational cost associated with the Bayesian inference is mitigated by the use of neural networks (NNs) as emulators of the RBC model output. This approach enables the simultaneous inference of all material properties in the employed RBC model. In particular, the SFS (parameterized by its reduced volume), shear (both linear and non-linear components), and bending moduli are inferred from experimental data of RBCs in equilibrium (20) and under stretching (21,22). In turn, the membrane viscosity is inferred from experiments of RBC relaxation after elongation (23).

Predictions of the fully calibrated model are validated against experimental data coming from complex flow conditions that were not part of the inference. Specifically, the calibrated model captures the velocity and elongation of RBCs flowing in a microtube (24), the tank-treading frequency (TTF), and inclination angle of RBCs in simple shear flows (25), and, most importantly, the critical shear stress between the tumbling and tank-treading motion of RBCs in shear flow (26). Our findings demonstrate, for the first time, the transferability of the inferred model, without problem-specific tuning, and its capability to predict complex flow configurations that were not part of the inference.

METHODS

RBC model

We model the RBC membrane as a surface whose dynamics evolve according to bending resistance of the lipid bilayer, shear and dilation elasticity of the cytoskeleton, and membrane viscosity. The shear and dilation elasticity are minimal at the SFS of the RBC, a state that is not known. The resistance to bending is described by the energy

$$U_{bending} = 2\kappa_b \oint H^2 dA, \tag{1}$$

where the integral is taken over the membrane, κ_b is the bending modulus, and H is the mean curvature of the membrane. The in-plane elastic energy accounts for the shear and dilation elasticity of the cytoskeleton,

$$U_{in-plane} = \frac{K_\alpha}{2} \oint \left(\alpha^2 + a_3\alpha^3 + a_4\alpha^4\right) dA_0 + \mu \oint \left(\beta + b_1\alpha\beta + b_2\beta^2\right) dA_0, \tag{2}$$

where the integral is taken over the SFS surface, α and β are the local dilation and shear strain invariants of the membrane, respectively; K_α is the dilation elastic modulus; μ is the shear elastic modulus; and the coefficients a_3, a_4, b_1, and b_2 are parameters that control the non-linearity of the membrane elasticity for large deformations (4).

The membrane is discretized into a triangle mesh composed of N_v vertices with positions $\mathbf{r}_i$, velocities $\mathbf{v}_i$, and mass m, $i = 1, 2, \ldots, N_v$, evolving according to Newton's law of motion. The bending energy described by Eq. 1 is discretized following Jülicher (27) and Bian et al. (28), and the in-plane energy is computed as described in Lim et al. (4). The forces arising from these energy terms are formed by the negative gradient of the energy with respect to the particle positions. The membrane viscosity is modeled through pairwise forces between particles sharing an edge in the triangle mesh. The viscous force exerted by particle j to particle i is given by (29)

$$\mathbf{f}_{ij}^{visc} = -\gamma\left(\mathbf{v}_{ij} \cdot \mathbf{e}_{ij}\right)\mathbf{e}_{ij}, \tag{3}$$

where γ is the friction coefficient, $\mathbf{v}_{ij} = \mathbf{v}_i - \mathbf{v}_j$, and $\mathbf{e}_{ij}$ is the unit vector between $\mathbf{r}_i$ and $\mathbf{r}_j$. The membrane viscosity depends linearly on the friction coefficient, $\eta_m = \gamma\sqrt{3}/4$. Finally, the constraints of preserving the area of the membrane and the volume of the cytosol are enforced through energy penalization terms,

Please cite this article in press as: Amoudruz et al., The stress-free state of human erythrocytes: Data-driven inference of a transferable RBC model, Biophysical Journal (2023), https://doi.org/10.1016/j.bpj.2023.03.019

$$U_{area} = k_A \frac{(A - A_0)^2}{A_0}, U_{volume} = k_V \frac{(V - V_0)^2}{V_0},$$

where A_0 and V_0 are the area and volume of the cell at rest and A and V are the area and volume of the cell, respectively. The coefficients k_A and k_V are chosen empirically with values that are large enough to enforce the conservation of the membrane area and volume of the RBC. More details on the discretization of the energies are presented in the supporting material.

The SFS of the RBC is parameterized by its reduced volume v; i.e., the volume of the SFS relative to that of a sphere with same area as the SFS. Following Lim et al. (4), the SFS is obtained by minimizing the energy of a membrane with bending resistance, shear, and dilation elastic energy with a sphere as reference state. The area of the SFS is constrained to that of a healthy RBC and the volume is parameterized by the reduced volume v (ratio of the volume with respect to that of a sphere with the same area). With v ranging from 0.65 to unity, this procedure results in biconcave shapes, oblates, and spheroids at low, intermediate, and high reduced volume, respectively (Fig. 1). We note that the value of this reduced volume is chosen arbitrarily in RBC models and accordingly affects their dynamics.

The parameters governing the RBC mechanics comprise the reduced volume of the SFS v, the shear modulus μ, the shear-hardening coefficient b_2, the bending modulus κ_b, and the membrane viscosity η_m. These parameters are calibrated from experimental datasets that we introduce in the next sections. The remaining parameters of the model are chosen as follows: the dilation elastic modulus is set to $K_\alpha = \mu$; the non-linear coefficients in the shear energy formulation are set to $a_3 = -1$, $a_4 = 8$, and $b_1 = 0.7$ (4); and the area and volume of the cells are fixed to $A_0 = 135 \quad \mu m^2$ and $V_0 = 94 \quad \mu m^3$, respectively (20).

Heterogeneous data and a probabilistic model for the RBC: transferable RBC

We link seven experimental datasets measured from three experimental conditions with the computational model using a hierarchical statistical framework. The first dataset corresponds to the measurements of the diameter D, maximal thickness h_{max}, and minimal thickness h_{min} of single cells at equilibrium, as reported by Evans and Fung (20). The second and third datasets are measurements of the two principal diameters of RBCs stretched by two micro-beads. The micro-beads are attached to the membrane at two opposite sides of the cell's rim and are pulled by forces of magnitude F_{ext} in opposite directions. The two largest principal diameters of the cells, D_{ax} and D_{tr}, are reported by Mills et al. (21) and Suresh et al. (22) against the stretching force magnitude F_{ext}. The remaining datasets were collected by Hochmuth et al. (23) from initially stretched RBCs relaxing to their equilibrium shape. The datasets consist in the ratio of the two principal diameters of the cells, D_{ax}/D_{tr} measured at constant time intervals.

We assume that each dataset is one realization of the random variable $\mathbf{y}_{\alpha,i}$ (called observable), where α denotes the experimental conditions (equilibrium, stretching, or relaxation) and i is the index of the dataset (we drop the indices in the remaining of this section to lighten the notations). The transferable RBC (t-RBC) model relates the computational model and its parameters to the probability distribution of the observable. The structure of the t-RBC model, represented as a directed acyclic graph (DAG), is shown on Fig. 2. We distinguish the parameters of the computational model, $\vartheta = (v,\mu,\kappa_b,b_2,\eta_m)$, from those of the error model (explained below), such as the standard deviation σ. In addition, we introduce the hyper-parameter $\boldsymbol{\psi}$, which is further discussed below.

The hierarchical structure of the t-RBC model represents two levels of uncertainty. First, the computational parameters $\boldsymbol{\vartheta_i}$ for each dataset i are drawn from a distribution parameterized by the hyper-parameter $\boldsymbol{\psi}$, $p(\boldsymbol{\vartheta_i}|\boldsymbol{\psi})$, representing the variability of the cells' properties. This variability is due to the origin of the cells (from different donors), the age of the cells, and the different experimental conditions. Second, for each dataset, the observable is assumed to be normally distributed around the output of the computational model. This second level of uncertainty reflects the measurement errors and the inaccuracy of the computational model. The measurement errors are modeled separately for each experimental condition, with parameters as shown in Fig. 2. We note that, in the case of the relaxation experiment, we introduced an intermediate variable, t_c, which is the relaxation time of the cell. This addition simplifies the inference procedure as the initial shape of the RBC in experiments is unknown. Instead, we assume that t_c depends on the RBC parameters only and is independent on the initial shape of the cell. This assumption allows us to estimate t_c from the computational model with an arbitrary initial stretched shape. The data are then modeled as an exponential decay with rate t_c^{-1} and additional parameters contained in ϑ_z. The exact dependencies between the random variables are detailed in the supporting material.

Offline surrogate of the computational model

The evaluation of the computational model for each experimental condition (cell equilibration, stretching, and relaxation), although relatively fast thanks to the high-performance implementation in Mirheo (30), remains computationally costly for performing Bayesian inference of the t-RBC model presented above. Instead, we replace the computational model during the Bayesian inference with an offline surrogate.

The surrogate is formed by three NNs, one for each experimental condition, that takes as input the computational parameters ϑ (and the stretching force magnitude F_{ext} for the stretching case) and outputs the observable of the computational model ((D, h_{min}, h_{max}) for the equilibration case, (D_{ax}, D_{tr}) for the stretching case, and t_c for the relaxation case). Each NN is composed of three hidden layers of 32 neurons and hyperbolic tangent

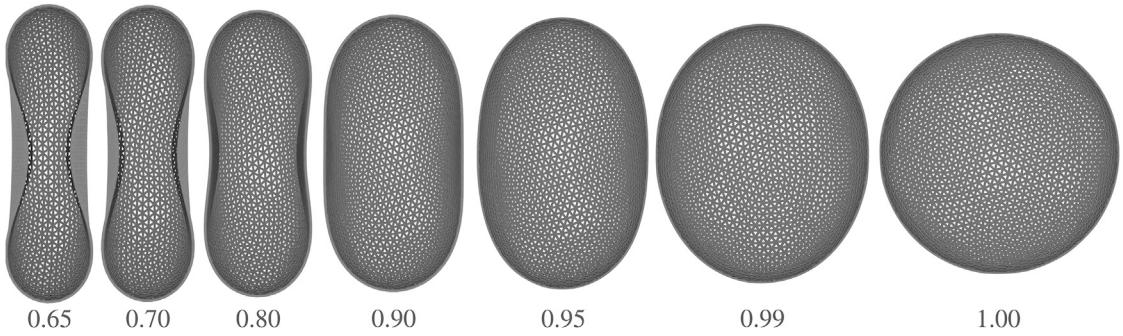

FIGURE 1 SFS shapes of different reduced volumes v (indicated below each shape). All shapes are axi-symmetric around the horizontal axis.

Please cite this article in press as: Amoudruz et al., The stress-free state of human erythrocytes: Data-driven inference of a transferable RBC model, Biophysical Journal (2023), https://doi.org/10.1016/j.bpj.2023.03.019

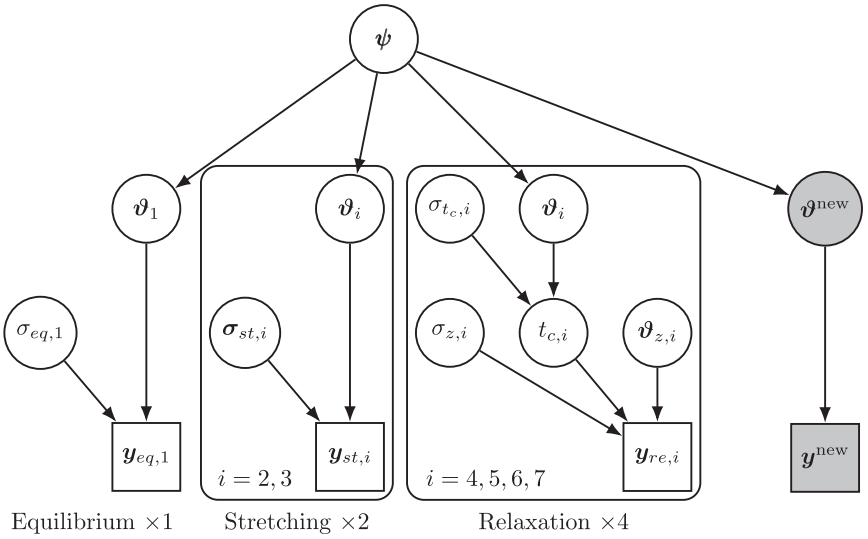

FIGURE 2 Structure of the t-RBC model, presented as a DAG. Rectangular and circular nodes are observed and unobserved quantities, respectively. The arrows represent the causal links between variables. Rounded rectangles are repeated depending on the number of datasets for each case. Shaded nodes are not part of the inference and are used to predict configurations that were not used during the inference phase.

activation gates. The training data were generated for 50,000 samples uniformly distributed in the input space of the surrogate. The corresponding observable values were then computed with the procedure described in Fig. 3 using the computational model. The NN parameters were then trained on these samples (split into 80% and 20% training and validation sets, respectively) to minimize the mean squared error between the NNs and the computational model outputs. The training was performed with the Adam optimizer and we used early stopping to avoid over-fitting. The prediction accuracy of the surrogate is shown in the supporting material.

RESULTS AND DISCUSSION

Bayesian inference

We infer the parameters of the RBC model from the combined experimental datasets using hierarchical Bayesian inference. The posterior distribution of the parameters is sampled using Bayesian annealed sequential important sampling (BASIS) (31), an unbiased version of transitional Markov chain Monte-Carlo (TMCMC) (32). This sampling method does not rely on the gradient of the model with respect to the parameters. In this situation, regions of constant likelihood lead to poor sampling (33). In turn, we eliminate the parameters that are inert for the respective experimental condition. We performed a sensitivity analysis of the model output with respect to the parameters in the supporting material. The results indicate that the combination of the three experimental cases chosen in this study are complementary for the inference of the cell parameters: the equilibrium shape is sensitive to v and FvK (where FvK $= \mu A_0/4\pi\kappa_b$ is the Föppl-von Kármánn number), the stretched cell diameters vary mainly with μ and b_2 (and v and FvK at low stretching forces), and the relaxation characteristic time is sensitive to μ and η_m.

The parameters of the t-RBC model are sampled as described in the supporting material using the Korali framework (34). The resulting posterior distribution of the RBC parameters, $p(\boldsymbol{\vartheta}^{\text{new}}|\mathbf{d})$, is shown on Fig. 4, with corresponding mean, median, maximal likelihood (ML) and maximal a posteriori (MAP) values reported in Table 1. All distributions have a clear peak with relatively high uncertainties around the MAP, due to the heterogeneity of the datasets.

The inferred shear modulus has a mean at $\mu = 4.99$ μN m^{-1}, which is within the range of values used in previous studies: 6.3 μN m^{-1} (35,36), 2.42 μN m^{-1} (37), 4.5 μN m^{-1} (38). Similarly, the inferred bending modulus is consistent with the values used in previous studies ($\kappa_b = 2.4 \times 10^{-19}$J (35), (36), 1.43×10^{-19}J (37), 3.0×10^{-19}J (38)). In addition, the inferred membrane viscosity is close to that found in Wälchli et al. (39) (0.63Pa s μm) and in Hochmuth et al. (23) (0.6 – 0.8Pa s μm). The parameter b_2 is found higher than in Lim et al. (4). However, the cell deformations were most likely smaller in the latter study than in the cell-stretching experiments that were used for the inference.

The inferred reduced volume of the SFS has a mean around $v = 0.94$, which suggests that the SFS is more likely an oblate than the biconcave shape, based on these experimental datasets. This value is close to those used in previous studies ($v = 0.95$ (5), $v = 0.96$ (9), (7,8), $v = 0.997$ (6)). Furthermore, the range of values obtained from the Bayesian inference agrees with the conclusions of Lim et al. (4), who showed that $0.925 \leq v \leq 0.976$ to reproduce the stomatocyte-discocyte-echinocyte (SDE) sequence observed when changing the bending properties of the lipid bilayer of the membrane. Similarly, Geekiyanage et al. (40) concluded that the reduced volume of the SFS is around $v = 0.94$ to obtain the SDE sequence. We note that the result of Lim et al. (4) was obtained with predefined values of the mechanical properties of the membranes, whereas in the current work the mechanical properties of the membranes are inferred together with the

Please cite this article in press as: Amoudruz et al., The stress-free state of human erythrocytes: Data-driven inference of a transferable RBC model, Biophysical Journal (2023), https://doi.org/10.1016/j.bpj.2023.03.019

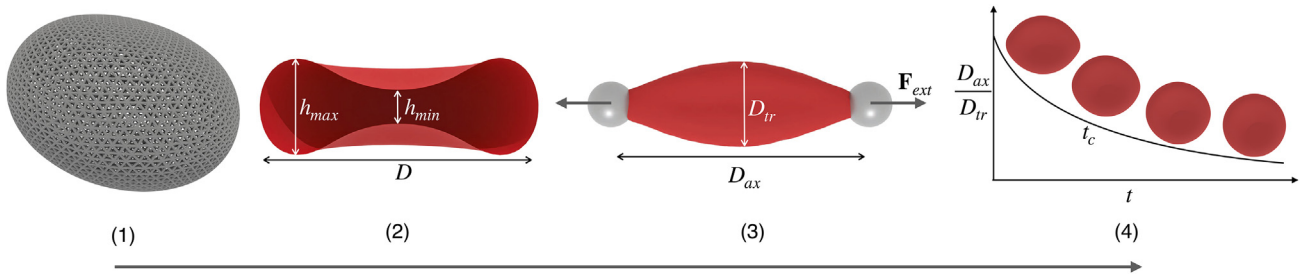

FIGURE 3 Sequence of simulations used to compute the output of all experiments for a set of parameters ϑ. (1) Generation of the SFS mesh, needed by all subsequent simulations. (2) Generation of the equilibrium shape. (3) Stretching of the equilibrated cell. (4) Relaxation of the stretched cell. To see this figure in color, go online.

SFS reduced volume. Furthermore, the studies that inferred the SFS reduced volume based on the SDE sequence did not consider the dynamics of the RBCs in dynamic flow conditions (4,40),

The inferred parameters are then tested against the experimental datasets used for the inference. Fig. 5 shows the predictions of the t-RBC model for one dataset for each experimental condition. The parameters used for the predictions are sampled from the probability distribution $p(\boldsymbol{\vartheta}_i|\mathbf{d})$, where $\mathbf{d}$ contains the seven datasets used for the inference. In all cases, the experimental data lie inside the credible intervals given by the t-RBC model.

Model generalization

Contrary to the one-at-a-time approach, a commonly used practice for validating RBC models (35,41,42), we test the predictive accuracy of the calibrated RBC model in configurations that were not seen during the inference. The posterior distribution of the parameters was inferred using simple experimental conditions where only one or two parameters had a significant effect on the output in each case. Here, the calibrated model is validated in complex dynamic situations, where multiple parameters affect the output, as shown in parametric studies found in the literature (details below). In particular, we test the model prediction on five quantities: the TTF, inclination angle, and threshold shear stress for tumbling-to-tank-treading transition of RBCs in simple shear flow, the elongation of RBCs flowing through a microtube, and their respective velocity against the applied pressure gradient. The TTF and inclination angle are known to be significantly affected by the membrane viscosity (43). The threshold shear stress for tumbling-to-tank-treading transition depends on the SFS (6,7), and the length of flowing RBCs in microtubes depends on the bending stiffness of the membrane (44). We emphasize that it is crucial to estimate the prediction capabilities of the model on data coming from conditions not seen during the inference phase to test the transferability of the model.

The following cases are substantially more expensive in terms of computations than those used to calibrate the model (each evaluation takes at least 24 h on a single P100 graphics processing unit). Therefore, instead of propagating the posterior distribution of the parameters through the computational model, we evaluate each quantity of interest with the mean estimates of the posterior distribution.

RBC in a circular microtube

Single RBCs flowing in straight microtubes adopt a steady parachute-like shape. The cell length l and velocity v_x depend on the flow rate and the radius R of the tube. A pressure difference Δp between the ends of the tube causes the solvent and the cell to flow. The tube has a length $L \gg R$ large enough that the cells reach an equilibrium shape before the measurements. The length and velocity of the cells, l and v_x, were recorded for different pressure gradients $\nabla p = \Delta p/L$ experimentally for $R = 3.30$ μm (24) and $R = 3.35$ μm (45). Simulations of this system are performed with the current calibrated model (using the mean

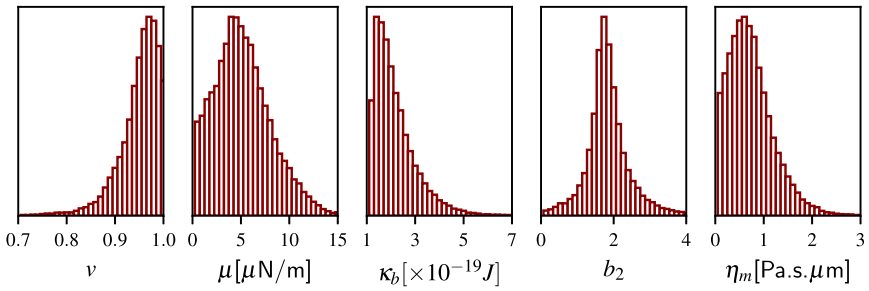

FIGURE 4 Posterior distribution of the RBC parameters $p(\boldsymbol{\vartheta}^{\mathrm{new}}|\mathbf{d})$. Only the marginal distributions are shown since the variables are independent. To see this figure in color, go online.

TABLE 1 Statistics on the posterior distribution of the parameters based on all the experimental datasets

	Mean	Median	ML	MAP	standard deviation
v	0.94	0.95	0.96	0.96	0.04
μ	4.99	4.68	4.60	4.60	2.24
κ_b	2.10	1.85	1.46	1.46	0.93
b_2	1.84	1.73	1.69	1.69	0.82
η_m	0.69	0.62	0.66	0.66	0.46

The parameters μ, κ_b, and η_m are expressed in $\mu N \quad m^{-1}$, $1 \times \ 10^{-19}$, and Pa s μm, respectively.

of the posterior distributions) for $R = 3.30 \quad \mu$m (see supporting material for details). The simulations show a good agreement with the experimental data (Fig. 6). The variability of the cell lengths in the experiments could be attributed to the variability in the mechanical properties of the cells but also to that of the cell sizes.

RBC in a linear shear flow

Single RBCs suspended in a linear shear flow exhibit rich dynamics. At low shear rates, the cells tumble (rotate in a rigid-like motion). Increasing the shear rate above a threshold value causes the cell membrane to tank tread: the cell adopts an elongated shape forming an angle θ with the flow direction, whereas the membrane rotates around the cell with a frequency f (the TTF). Below we present predictions of the t-RBC model for the inclination angle, the TTF, and the critical shear stress for tumbling to tank-treading transition. These predictions were obtained for a fixed cytosol viscosity (see Supporting Material). However, we remark that this quantity is known to depend on the hemoglobin concentration, which varies notably with the age of the cells, and it may be of importance to model this variation in further research (46).

Inclination angle

Measurements of inclination angles of tank-treading RBCs in simple shear flows have been reported by Fischer and Korzeniewski (25). The inclination angle θ obtained with the calibrated RBC model (with the mean estimate of the parameters) is shown against the shear rate $\dot{\gamma}$ on Fig. 7. The model predictions are within the values observed experimentally. In particular, for a solvent viscosity $\eta = 23.9$ mPa s, the model captures the trend of the experimental data; i.e., an increase of θ with $\dot{\gamma}$ followed by a decrease of θ above a critical shear rate. This trend is less pronounced at the lower solvent viscosity $\eta = 10.7$ mPa s, both experimentally and in the simulations.

Tank treading frequency

Fig. 8 shows the dimensionless TTF, $4\pi f/\dot{\gamma}$, of a tank-treading RBC suspended in a linear shear flow (with solvent viscosity $\eta = 28.9$ mPa s) for various shear rates $\dot{\gamma}$. The t-RBC model predictions are performed with the mean estimate of the parameters. Despite the complex dependency of the TTF on the computational parameters, the t-RBC model shows a good agreement with the TTF experimental data reported by Fischer (47). Furthermore, the biconcave shape of the cell is preserved in the tank-treading simulations, as observed experimentally (11) (see Fig. S2). However, we note that the biconcavity of the cell during tank treading is only reported qualitatively in experiments, and quantitative experimental data could help in further improving the calibration of the model.

Tumbling to tank-treading transitions in linear shear flow

RBCs in a linear shear flow undergo different regimes depending on the shear rate $\dot{\gamma}$ and solvent viscosity (49). At large shear rates, the cell orientation oscillates around a steady angle while the membrane rolls, or tank treads, around

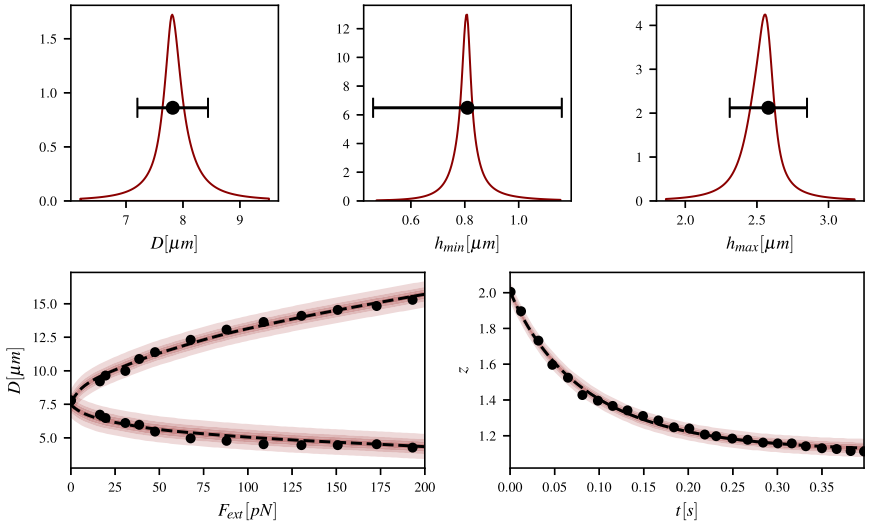

FIGURE 5 Forward predictions of the t-RBC model on the single-cell experiments. Top: probability distribution of the diameter (left), minimal thickness (middle), and maximal thickness (right) of an equilibrated cell. The symbols and error bars denote the measurements and corresponding standard deviations reported by Evans and Fung (20), respectively. Bottom left: cell diameters against the stretching force magnitude. Mean prediction (dashed line) and experimental data from Mills et al. (21) (symbols). The shaded regions denote the 50%, 75%, 90%, and 99% credible intervals of the predictions. Bottom right: ratio of the cell diameters $z = D_{ax}/D_{tr}$ against time of an initially stretched RBC. The symbols are the experimental data from Hochmuth et al. (23). To see this figure in color, go online.

Please cite this article in press as: Amoudruz et al., The stress-free state of human erythrocytes: Data-driven inference of a transferable RBC model, Biophysical Journal (2023), https://doi.org/10.1016/j.bpj.2023.03.019

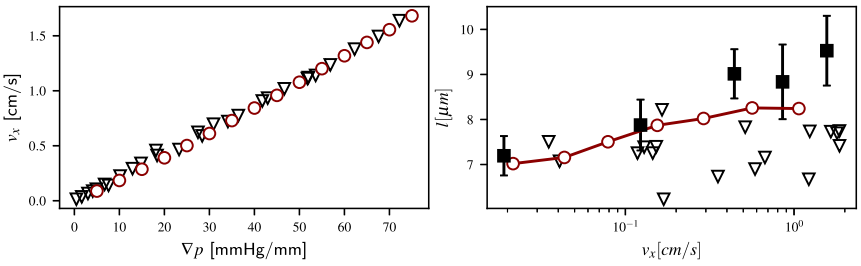

FIGURE 6 RBC flowing in a straight circular microtube of radius $R = 3.3$ μm. Left: velocity of the cell v_x against the applied pressure gradient ∇p. Experimental data from Tomaiuolo et al. (24) (triangles) and simulation results (circles). Right: length of the RBC l against the velocity v_x. Experimental data from Tomaiuolo et al. (24) and Hochmuth et al. (45) (squares and triangles, respectively) and simulation results (open circles). Error bars in the experiments indicate the standard deviation. To see this figure in color, go online.

the cell. In contrast, RBCs rotate as a rigid object, or tumble, when the shear rate is below a critical value. The critical shear stress $\tau = \dot{\gamma}\eta$ has been measured experimentally by Abkarian et al. (48) and Fischer and Korzeniewski (26) for different solvent viscosity η. We performed numerical simulations with the calibrated model at different shear rates for several viscosity values η. For a given solvent viscosity, the flow regime of the cell (tumbling or tank treading) was reported for several shear rates. The highest and lowest shear rates at which the RBC tumbles and tank treads, respectively, are reported in Fig. 8. The model predictions are in good agreement with experimental data. As in the experimental data, the critical shear stress decreases sharply for solvent viscosity below 30 mPa s and reaches a plateau above that viscosity. Note that we show only the transitions for the discocytes in the data from Fischer and Korzeniewski (26). The data points marked with crosses at $\eta = 23.9$ mPa s are from cells that previously underwent shape transitions, possibly modifying their mechanical properties. This observation probably explains the deviations between the shear stress obtained from experiments and that obtained from the simulations at this particular viscosity.

Limitations of the study

To minimize the computational cost of inference, we have fixed several parameters to specific values. Specifically, the membrane model assumes zero spontaneous curvature (Eq. 1), which typically results from differences in monolayer compositions found *in-vivo*. However, discocytes, as shown in Figure 2.45 of Lim et al. (4), have been found to exhibit a spontaneous curvature close to zero and we therefore ignored the spontaneous curvature in the current work. Similarly, the area and volume of the RBCs exhibit a distribution that reflects the variability and aging of the cells. Although it is possible to include these variations in the statistical model, doing so would increase the complexity of the model and the computational cost for inference. For similar reasons, we fixed the ratio K_α/μ as in Economides et al. (1). Although this choice is arbitrary, the current model accurately predicts various flow conditions. The value of these parameters should ideally be inferred from additional experimental data and can be the subject of future research.

CONCLUSIONS

We introduce a t-RBC model that quantifies the visco-elastic membrane parameters and the SFS of healthy RBCs through Bayesian inference. The t-RBC model takes into account the cell heterogeneity, the measurement errors, and the computational model inaccuracies. The model parameters were calibrated on seven datasets comprising measurements of RBC dimensions at equilibrium, RBC elongation under stretching forces, and RBC relaxation time. The posterior distribution of the parameters has a relatively large standard deviation that possibly reflects the variability of mechanical properties among RBCs. The reduced volume of the SFS takes values that suggest that the cytoskeleton of RBCs, in its unstressed state, has an oblate shape. The calibrated shear modulus, bending modulus, and viscosity of the membrane were found to be in good agreement with previous studies, and we provide uncertainty on these parameters.

The calibrated model accurately predicts complex, single-cell dynamics and agrees well with experimental data that were not used during the inference phase. In particular, the calibrated model accurately predicts the velocity and

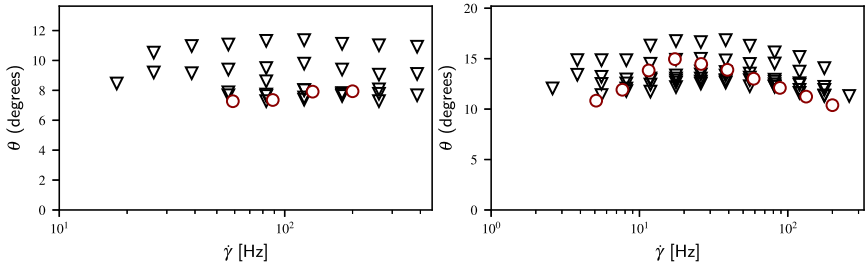

FIGURE 7 Mean inclination angle of tank-treading RBCs in a linear shear flow against the shear rate $\dot{\gamma}$. The triangles are data from Fischer and Korzeniewski (25) and the empty circles are the simulation predictions obtained with the mean parameters of the posterior distributions. The left and right figures correspond to solvent viscosities $\eta = 10.7$ mPa s and $\eta = 23.9$ mPa s, respectively. To see this figure in color, go online.

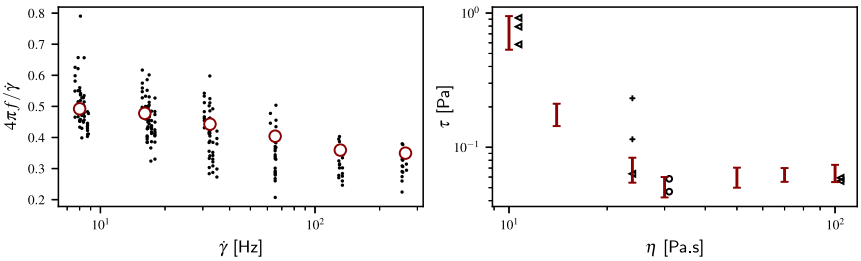

FIGURE 8 Left: TTF (normalized by the angular frequency of a sphere in a shear flow) of the RBC in a linear shear flow against the shear rate $\dot{\gamma}$, with a solvent viscosity $\eta = 28.9$ mPa s. Experimental data from Fischer (47) (dots) and simulation results with the mean parameters (open circles). Right: critical shear stress $\tau = \dot{\gamma}\eta$ of the tumbling to tank-treading transition against the solvent viscosity η. Experimental data from Fischer and Korzeniewski (26) (triangles and crosses) and Abkarian et al. (48) (circles), simulation results (bars). The crosses correspond to cells that underwent shape transitions due to chemicals. To see this figure in color, go online.

length of cells flowing in narrow tubes, the inclination angle, and TTF of tank-treading cells in linear shear flows and the critical shear stress of the tumbling to tank-treading motion of RBCs in linear shear flows. We emphasize that the aforementioned quantities highly depend on the visco-elastic properties of the RBC model, as demonstrated in numerous parametric studies in the literature. The transferability of the proposed t-RBC model makes it a candidate of choice for predicting the dynamics of RBCs in previously unseen flow configurations that involve large deformations and/or complex dynamics. In addition, the variability of the inferred parameters can be used to provide a more realistic description of blood flows with many cells, each cell having parameters drawn from the posterior density. This approach would model the heterogeneity of the cells in blood. The samples from the posterior density of the parameters are available online, together with the code used to produce the results of this study (50).

SUPPORTING MATERIAL

Supporting Material can be found online at https://doi.org/10.1016/j.bpj.2023.03.019.

AUTHOR CONTRIBUTIONS

A.E., L.A., and P.K. designed the research. L.A. and A.E. ran the RBC simulations. L.A., A.E., and G.A. performed the Bayesian inference. L.A. built the surrogate model. L.A., A.E., and P.K. interpreted the results. L.A., A.E., G.A., and P.K. wrote the article.

ACKNOWLEDGMENTS

We would like to thank Xin Bian and Sergey Litvinov for their invaluable insights on RBC modeling and simulations. We acknowledge support by The European High-Performance Computing Joint Undertaking (EuroHPC) Grant DCoMEX (956201-H2020-JTI-EuroHPC-2019-1) and computational resources granted by the Swiss National Supercomputing Center (CSCS) under the project ID s929.

DECLARATION OF INTERESTS

The authors declare no competing interests.

REFERENCES

1. Economides, A., G. Arampatzis, …, P. Koumoutsakos. 2021. Hierarchical Bayesian uncertainty quantification for a model of the red blood cell. *Phys. Rev. Appl.* 15:034062.
2. Caro, C. G., T. J. Pedley, …, K. H. Parker. 2011. The Mechanics of the Circulation, second edition. Cambridge University Press.
3. Freund, J. B. 2014. Numerical simulation of flowing blood cells. *Annu. Rev. Fluid Mech.* 46:67–95.
4. Gerald Lim, H. W., M. Wortis, and R. Mukhopadhyay. 2008. Red blood cell shapes and shape transformations: Newtonian mechanics of a composite membrane. *Soft Matter.* 4:139–204.
5. Khairy, K., J. Foo, and J. Howard. 2010. Shapes of red blood cells: comparison of 3D confocal images with the bilayer-couple model. *Cell. Mol. Bioeng.* 1:173–181.
6. Cordasco, D., A. Yazdani, and P. Bagchi. 2014. Comparison of erythrocyte dynamics in shear flow under different stress-free configurations. *Phys. Fluids.* 26:041902.
7. Peng, Z., A. Mashayekh, and Q. Zhu. 2014. Erythrocyte responses in low-shear-rate flows: effects of non-biconcave stress-free state in the cytoskeleton. *J. Fluid Mech.* 742:96–118.
8. Peng, Z., S. Salehyar, and Q. Zhu. 2015. Stability of the tank treading modes of erythrocytes and its dependence on cytoskeleton reference states. *J. Fluid Mech.* 771:449–467.
9. Mauer, J., S. Mendez, …, D. A. Fedosov. 2018. Flow-induced transitions of red blood cell shapes under shear. *Phys. Rev. Lett.* 121:118103.
10. Fischer, T. M. 2004. Shape memory of human red blood cells. *Biophys. J.* 86:3304–3313.
11. Dupire, J., M. Socol, and A. Viallat. 2012. Full dynamics of a red blood cell in shear flow. *Proc. Natl. Acad. Sci. USA.* 109:20808–20813.
12. Švelc, T., and S. Svetina. 2012. Stress-free state of the red blood cell membrane and the deformation of its skeleton. *Cell. Mol. Biol. Lett.* 17:217–227.
13. Lee, J. C., D. T. Wong, and D. E. Discher. 1999. Direct measures of large, anisotropic strains in deformation of the erythrocyte cytoskeleton. *Biophys. J.* 77:853–864.
14. Levant, M., and V. Steinberg. 2016. Intermediate regime and a phase diagram of red blood cell dynamics in a linear flow. *Phys. Rev. E.* 94:062412–062414.
15. Tsubota, K. I., S. Wada, and H. Liu. 2014. Elastic behavior of a red blood cell with the membrane's nonuniform natural state: equilibrium shape, motion transition under shear flow, and elongation during tank-treading motion. *Biomech. Model. Mechanobiol.* 13:735–746.
16. Li, J., M. Dao, C. T. Lim, and S. Suresh. 2005. Spectrin-level modeling of the cytoskeleton and optical tweezers stretching of the erythrocyte. *Biophys. J.* 88:3707–3719.
17. Cordasco, D., and P. Bagchi. 2017. On the shape memory of red blood cells. *Phys. Fluids.* 29:041901–041918.

18. Reichel, F., J. Mauer, …, D. A. Fedosov. 2019. High-throughput microfluidic characterization of erythrocyte shapes and mechanical variability. *Biophys. J.* 117:14–24.
19. Arampatzis, G., D. Wälchli, …, P. Koumoutsakos. 2018. Langevin diffusion for population based sampling with an application in Bayesian inference for pharmacodynamics. *SIAM J. Sci. Comput.* 40:B788–B811.
20. Evans, E., and Y. C. Fung. 1972. Improved measurements of the erythrocyte geometry. *Microvasc. Res.* 4:335–347.
21. Mills, J. P., L. Qie, …, S. Suresh. 2004. Nonlinear Elastic and Viscoelastic Deformation of the Human Red Blood Cell with Optical Tweezers, 1. MCB-TECH SCIENCE PRESS-, pp. 169–180.
22. Suresh, S., J. Spatz, …, T. Seufferlein. 2005. Connections between single-cell biomechanics and human disease states: gastrointestinal cancer and malaria. *Acta Biomater.* 1:15–30.
23. Hochmuth, R. M., P. R. Worthy, and E. A. Evans. 1979. Red cell extensional recovery and the determination of membrane viscosity. *Biophys. J.* 26:101–114.
24. Tomaiuolo, G., M. Simeone, …, S. Guido. 2009. Red blood cell deformation in microconfined flow. *Soft Matter.* 5:3736–3740.
25. Fischer, T. M., and R. Korzeniewski. 2015. Angle of inclination of tank-treading red cells: dependence on shear rate and suspending medium. *Biophys. J.* 108:1352–1360.
26. Fischer, T. M., and R. Korzeniewski. 2013. Threshold shear stress for the transition between tumbling and tank-treading of red blood cells in shear flow: dependence on the viscosity of the suspending medium. *J. Fluid Mech.* 736:351–365.
27. Jülicher, F. 1996. The morphology of vesicles of higher topological genus: conformal degeneracy and conformal modes. *J. Phys. II France.* 6:1797–1824.
28. Bian, X., S. Litvinov, and P. Koumoutsakos. 2020. Bending models of lipid bilayer membranes: spontaneous curvature and area-difference elasticity. *Comput. Methods Appl. Mech. Eng.* 359:112758.
29. Fedosov, D. A. 2010. Multiscale Modeling of Blood Flow and Soft Matter. Ph.D. thesis.
30. Alexeev, D., L. Amoudruz, …, P. Koumoutsakos. 2020. Mirheo: high-performance mesoscale simulations for microfluidics. *Comput. Phys. Commun.* 254:107298.
31. Wu, S., P. Angelikopoulos, …, P. Koumoutsakos. 2017. Bayesian annealed sequential importance sampling (BASIS): an unbiased version of transitional Markov chain Monte Carlo. *ASCE-ASME J. Risk Uncertain. Eng. Sys. B.* 4:011008.
32. Ching, J., and Y.-C. Chen. 2007. Transitional Markov chain Monte Carlo method for Bayesian model updating, model class selection, and model averaging. *J. Eng. Mech.* 133:816–832.
33. Raue, A., C. Kreutz, …, J. Timmer. 2013. Joining forces of Bayesian and frequentist methodology: a study for inference in the presence of non-identifiability. *Philos. Trans. A Math. Phys. Eng. Sci.* 371:20110544.
34. Martin, S. M., D. Wälchli, …, P. Koumoutsakos. 2021. Korali: efficient and scalable software framework for Bayesian uncertainty quantification and stochastic optimization. *Comput. Method. Appl. Mech. Eng.* 389:114264.
35. Fedosov, D. A., B. Caswell, and G. E. Karniadakis. 2010. Systematic coarse-graining of spectrin-level red blood cell models. *Comput. Methods Appl. Mech. Eng.* 199:1937.
36. Fedosov, D. A., B. Caswell, and G. E. Karniadakis. 2010. A multiscale red blood cell model with accurate mechanics, rheology, and dynamics. *Biophys. J.* 98:2215–2225.
37. Turlier, H., D. A. Fedosov, …, T. Betz. 2016. Equilibrium physics breakdown reveals the active nature of red blood cell flickering. *Nat. Phys.* 12:513–519.
38. Yazdani, A., and G. E. Karniadakis. 2016. Sub-cellular modeling of platelet transport in blood flow through microchannels with constriction. *Soft Matter.* 12:4339–4351.
39. Wälchli, D., S. M. Martin, …, P. Koumoutsakos. 2020. Load balancing in large scale Bayesian inference. *In* Proceedings of the Platform for Advanced Scientific Computing Conference – PASC '20 ACM.
40. Geekiyanage, N. M., M. A. Balanant, …, Y. Gu. 2019. A coarse-grained red blood cell membrane model to study stomatocyte-discocyte-echinocyte morphologies. *PLoS One.* 14:e0215447.
41. Kotsalos, C., J. Latt, and B. Chopard. 2019. Bridging the computational gap between mesoscopic and continuum modeling of red blood cells for fully resolved blood flow. *J. Comput. Phys.* 398:108905.
42. Dupin, M. M., I. Halliday, …, L. L. Munn. 2007. Modeling the flow of dense suspensions of deformable particles in three dimensions. *Phys. Rev. E Stat. Nonlin. Soft Matter Phys.* 75:066707.
43. Yazdani, A., and P. Bagchi. 2013. Influence of membrane viscosity on capsule dynamics in shear flow. *J. Fluid Mech.* 718:569–595.
44. Noguchi, H., and G. Gompper. 2005. Shape transitions of fluid vesicles and red blood cells in capillary flows. *Proc. Natl. Acad. Sci. USA.* 102:14159–14164.
45. Hochmuth, R. M., R. N. Marple, and S. P. Sutera. 1970. Capillary blood flow: I. Erythrocyte deformation in glass capillaries. *Microvasc. Res.* 2:409–419.
46. Chien, S., S. Usami, and J. F. Bertles. 1970. Abnormal rheology of oxygenated blood in sickle cell anemia. *J. Clin. Invest.* 49:623–634.
47. Fischer, T. M. 2007. Tank-tread frequency of the red cell membrane: dependence on the viscosity of the suspending medium. *Biophys. J.* 93:2553–2561.
48. Abkarian, M., M. Faivre, and A. Viallat. 2007. Swinging of red blood cells under shear flow. *Phys. Rev. Lett.* 98:188302–188305.
49. Yazdani, A. Z. K., and P. Bagchi. 2011. Phase diagram and breathing dynamics of a single red blood cell and a biconcave capsule in dilute shear flow. *Phys. Rev. E Stat. Nonlin. Soft Matter Phys.* 84:026314.
50. Amoudruz, L. 2022. cselab/tRBC-UQ: v1.0.0. Preprint at Zendo. https://doi.org/10.5281/zenodo.7320187.